https://doi.org/10.5194/egusphere-2025-707
Preprint. Discussion started: 26 February 2025

Stabilized two-phase material point method for hydromechanical coupling problems in solid-fluid porous media

Xiong Tang[1, 2, 3], Wei Liu[1, 2], Siming He[1, 2], Lei Zhu[1, 2], Michel Jaboyedoff[3], Huanhuan Zhang[1, 2], Yuqing Sun[1, 2], Zenan Huo[3]

[1] Institute of Mountain Hazards and Environment, Chinese Academy of Sciences, Chengdu 610041, China

[2] University of Chinese Academy of Sciences, Beijing 100049, China

[3] Analysis Group, Institute of Earth Sciences, University of Lausanne, CH 1015 Lausanne, Switzerland

Correspondence: Wei Liu (spon@imde.ac.cn), Siming He (hsm@imde.ac.cn)

Abstract. For the hydromechanically coupling of solid-fluid porous media, this study presents an explicit stabilized two phase MPM formulation based on the one-point two-phase MPM scheme. To mitigate the spurious pore pressure and maintain the numerical stability, the stabilized techniques including the strain smoothing method and the multi-field variational principle are implemented in the proposed formulation. The strain smoothing technique is used to smooth the volumetric strain rate, and the calculation of the pore pressure increasement at particles is based on the multi-field variational principle. Four numerical examples are performed to evaluate the performance of the proposed formulation. With its effective and easy implemented stabilized techniques, the proposed formulation provides stable and reliable outcomes that well align with analytical solutions and results from other approaches, offering extensively validation that the proposed two phase MPM formulation is an effective and reliable approach for the simulation of solid-fluid porous media under both static and dynamic conditions.

1 Introduction

The hydromechanically coupling of solid-fluid porous media widely presents in

https://doi.org/10.5194/egusphere-2025-707
Preprint. Discussion started: 26 February 2025

nature and engineering, from natural processes like rainfall-induced landslide and earthquake-induced liquefaction, to coastal dike-breaking and offshore foundations (Jerolmack and Daniels, 2019; Zhan et al., 2025; Guan and Shi, 2023). Due to the practical importance, reproducing and understanding the physical nature of such a two-phase system have attracted strong research interests across many scientific and engineering disciplines, which has become increasingly recognized with recent advances in both observational and simulation tools(Li et al., 2023; Taylor-Noonan et al., 2022; Pudasaini and Mergili, 2019). While the numerical modeling of this two-phase coupling system is still a significant challenge for researchers in many disciplines alike.

In soil-fluid coupling problems, the motion of each constituent is governed by stress distributions, external gravity forces and interaction forces (Pudasaini and Mergili, 2019; Baumgarten and Kamrin, 2018; Bandara and Soga, 2015). To better simulate this two-phase system, various numerical methods have been proposed, including the smoothed particle hydrodynamics (SPH) method (Lian et al., 2023; Chen et al., 2023), the particle finite element method (Yuan et al., 2022; Jin and Yin, 2022), and the material point method (MPM) (Bandara and Soga, 2015; Bandara et al., 2016; Jassim et al., 2013; Yerro et al., 2015; Wyser et al., 2020). Among these methods, MPM has been shown to be both useful and efficient for simulating large deformation problems with history-dependent materials. Originated from the particle-in-cell (PIC) method, MPM is a hybrid Euler-Lagrangian method which has significant advantages in dealing with large deformation problems (Li et al., 2020; Zhao et al., 2023; Fernández et al., 2023). In MPM, a continuum body is discretized by a group of material points carrying all physical information like displacement, velocity, stress, strain, etc. At each time step, the physical information at particles is interpolated to the background mesh node, which is essentially a Eulerian mesh, and then the governing equations can be solved on it. Subsequently, the solution is re-interpolated to each material particle to update the physical information. The original background mesh can be used again in the new time step, which can eliminate the mesh distortion problem in Lagrangian method, and the accuracy of the solution for large deformation problem

https://doi.org/10.5194/egusphere-2025-707
Preprint. Discussion started: 26 February 2025

can be guaranteed (Fig. 1). Currently, various coupling MPM formulations have been proposed (i.e. the one-point or two-point schemes (Bandara and Soga, 2015; Jassim et al., 2013), the solid displacement-fluid pressure or solid velocity-fluid velocity formulation (Zhang et al., 2009; Lei et al., 2020)) and have been widely used in two-phase coupling problems and engineering applications (Du et al., 2023; Ceccato et al., 2024; Shen et al., 2024; Zheng et al., 2024a; Yamaguchi et al., 2023; Zheng et al., 2024b; Zhan et al., 2025).

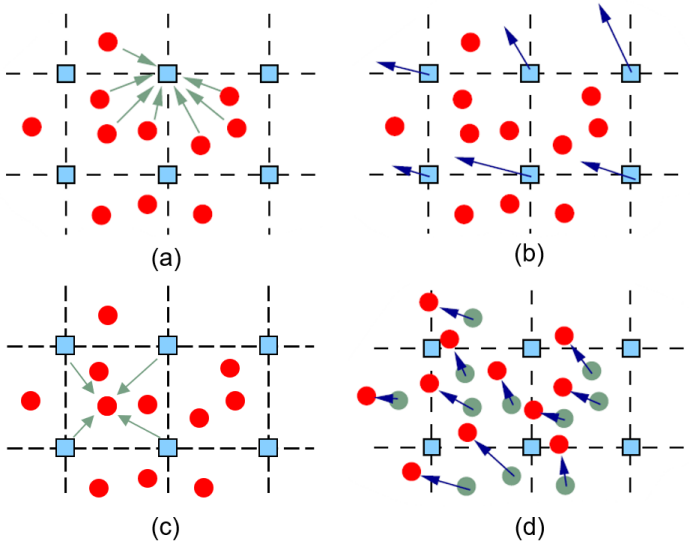

Figure 1. Standard algorithm of MPM: (a) interpolating information from particles to nodes; (b) solving governing equations on nodes; (c) interpolating information from nodes to particles; (d) update particles information.

However, the standard MPM formulation usually employs low-order shape functions within an explicit time integration scheme for simplicity and efficiency, which suffers from the cell-crossing error and the volumetric locking when applied to coupled hydromechanical problems (Li et al., 2024; Sang et al., 2024). The cell-crossing error during particle movement arises from the use of low-order shape functions, which have discontinuous gradients between background cells. To address this issue, higher-order interpolation functions with continuous gradients across elements can be employed, such as the Generalized Interpolation Material Point (GIMP) method

https://doi.org/10.5194/egusphere-2025-707
Preprint. Discussion started: 26 February 2025

(Bardenhagen and Kober, 2004), the B-spline method (De Vaucorbeil et al., 2020) and the Convected Particle Domain Interpolation (CPDI) (Wang et al., 2023b). Due to the low compressibility of pore fluid and limited permeability, the high stiffness of the pore fluid and low permeability will lead to volumetric locking and erroneous strain, which may not only result in undesired pore pressure oscillation, but also render the simulation highly unstable. Various numerical stabilization techniques have been implemented in MPM to solve this issue, including the reduce integration (Bandara and Soga, 2015; Zheng et al., 2021), the B-bar approach (Wang et al., 2018; Tang et al., 2024), the nodal or cell smoothing method (Lei et al., 2020; Wang et al., 2023a), the fractional stepping method (Kularathna et al., 2021; Jassim et al., 2013), the polynomial pressure projection method (Zhao and Choo, 2020), the multi-field variational principle (Liu et al., 2020; Zheng et al., 2021; Tang et al., 2024; Zheng et al., 2022), and coupling with other algorithms (Baumgarten et al., 2021; Li et al., 2024; Tran et al., 2023; Sang et al., 2024). Although these techniques produce results that overcome volumetric locking and reduce pore pressure oscillation, some are conditionally stable, and some require significant modifications of the existing MPM algorithm, leading to additional computation cost and difficulty (Lei et al., 2020; Li et al., 2024). Therefore, their usage should depend on the specific problem at hand. More the features and limitations of these techniques can be found in the summary of Li et al. (Li et al., 2024) and Sang et al. (Sang et al., 2024).

Here, based on the one-point two-phase MPM scheme (Jassim et al., 2013), we proposes an explicit stabilized two-phase MPM formulation for both static and dynamic analyses of solid-fluid porous media. To avert the volumetric locking and maintain the numerical stability, the stabilized techniques including the strain smoothing method (Mast et al., 2012) and the multi-field variational principle (Chen et al., 2018) have been implemented in the proposed formulation. The strain smoothing method is employed to smooth the volumetric strain rate, and the calculation of the pore pressure increasement at particles is based on the multi-field variational principle for accuracy and stability. The spurious pore pressure oscillation can be well mitigated during pore pressure calculation and interpolation. With these

https://doi.org/10.5194/egusphere-2025-707
Preprint. Discussion started: 26 February 2025

effective and easy implemented techniques, the volumetric locking can be significantly eliminated under both static and dynamic conditions. The study is organized as follows. First, the governing equations for two-phase flow are briefly introduced in Section 2. The numerical implementation of the proposed formulation and the stabilized techniques are presented in section 3. And then four numerical examples for the verification of the proposed method are performed and analyzed in section 4. Finally, discussion and conclusion are drawn in the last section.

2 Governing equations

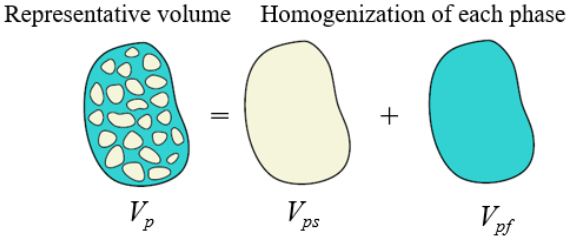

Figure 2. Sketch of material point composition in single-point-two-phase MPM model (Kularathna et al., 2021).

In one-point two-phase MPM formulation, according to the theory of mixture (Baumgarten and Kamrin, 2018), the representative volume (RVE) V_p of a particle material particle is a summation of solid phase volume V_{sp} and fluid phase volume V_{fp}, and each phase (solid, fluid) in the RVE can be characterized by its volume fraction (Fig. 2). The apparent density of each phase is characterized by the intrinsic density with the volume fraction, which reads,

$$\bar{\rho}_s = \varphi \rho_s, \ \bar{\rho}_f = n \rho_f \tag{1}$$

where φ is the solid volume fraction, n is the porosity, ρ_s and ρ_f are the intrinsic density of solid and fluid, respectively; $\bar{\rho}_s$ and $\bar{\rho}_f$ are the apparent density of solid and fluid, respectively.

2.1 Mass conservation equations

The mass conservations in a part of the solid/fluid phase continuum in Lagrangian

https://doi.org/10.5194/egusphere-2025-707
Preprint. Discussion started: 26 February 2025

description are expressed as,

$$\frac{D^s \bar{\rho}_s}{\mathrm{D}t} + \bar{\rho}_s \nabla \cdot \mathbf{v}_s = 0 \tag{2}$$

$$\frac{D^f \bar{\rho}_f}{Dt} + \bar{\rho}_f \nabla \cdot \mathbf{v}_f = 0 \tag{3}$$

where $\mathbf{v}_s$, $\mathbf{v}_f$ are the velocity of solid and fluid phases in their reference frame, respectively. In microscale, the solid grain is assumed to be incompressible, so ρ_s is constant. However, $\bar{\rho}_s$ will change when the solid phase compacts or dilates due to the deformation of the solid skeleton structure. Therefore, a simple expansion of Eq. (2) using the definition of porosity yields an expression for the change rate of the local measure of porosity,

$$\frac{D^s n}{Dt} = (1-n)\nabla \cdot \mathbf{v}_s \tag{4}$$

In one-point two-phase MPM formulation, all constituents are represented by the same Lagrangian material point in the current configuration. The material time derivative of the fluid phase with respect to the motion of the solid phase is described as follows,

$$\frac{D^f}{Dt} = \frac{D^s}{Dt} + (\mathbf{v}_f - \mathbf{v}_s) \cdot \nabla \tag{5}$$

So, Eq. (3) can be expressed as,

$$\frac{D^s \bar{\rho}_f}{Dt} + (\mathbf{v}_f - \mathbf{v}_s) \cdot \nabla \bar{\rho}_f + \bar{\rho}_f \nabla \cdot \mathbf{v}_f = 0 \tag{6}$$

And Eq. (6) can be further written as,

$$n\frac{D^s \rho_f}{Dt} + \rho_f \frac{D^s n}{Dt} + (\mathbf{v}_f - \mathbf{v}_s) \cdot \nabla n\rho_f + n\rho_f \nabla \cdot \mathbf{v}_f = 0 \tag{7}$$

Assuming the fluid phase is barotropic, density variation in a barotropic fluid obeys the following relationship,

$$\frac{1}{\rho_f}\frac{D^s \rho_f}{Dt} = \frac{1}{K_f}\frac{D^s p_f}{Dt} \tag{8}$$

where K_f is the bulk modulus of fluid, p_f is the pore fluid pressure.

Combining with Eq. (4) and neglecting spatial variations in density and porosity, the pore pressure change rate can be obtained,

$$\frac{D^s p_f}{Dt} = -\frac{K_f}{n}[(1-n)\nabla \cdot \mathbf{v}_s + n\nabla \cdot \mathbf{v}_f] \tag{9}$$

https://doi.org/10.5194/egusphere-2025-707
Preprint. Discussion started: 26 February 2025

2.2 Momentum conservation equations

The momentum conservation equations for each continuum phase are given as,

$$\bar{\rho}_s \frac{D^s \mathbf{v}_s}{Dt} = \bar{\rho}_s \mathbf{b} - f_b - f_d + \nabla \cdot \boldsymbol{\sigma}_s \tag{10}$$

$$\bar{\rho}_f \frac{D^f \mathbf{v}_f}{Dt} = \bar{\rho}_f \mathbf{b} + f_b + f_d + \nabla \cdot \boldsymbol{\sigma}_f \tag{11}$$

where $\mathbf{b}$ is the body force, which is equal to the gravitational acceleration; f_b and f_d are the buoyant force and inter-phase body force, respectively; $\boldsymbol{\sigma}_s$ and $\boldsymbol{\sigma}_f$ are the solid and fluid stress, respectively. Due to the viscous effects, a flow through porous media results in a drag force, which can be considered as a body force enforced on one phase from the other phase. The classic Darcy's law describes a linear drag force as,

$$f_d = \frac{n\bar{\rho}_f g}{K_s}(\mathbf{v}_s - \mathbf{v}_f) \tag{12}$$

where K_s, in the unit of m/s, is the hydraulic conductivity ($K_s = \rho_f g k/\mu_f$, where k is intrinsic permeability in the unit of m^2 and μ_f is the dynamic viscosity of fluid). This linear relation has been employed in several studies (Zhan et al., 2023; Liu et al., 2017) to model the drag force in saturated porous media when the pore flows are in the laminar flow range with a relatively low Reynolds number. While, the buoyant force, f_b, which yields the form for immiscible mixtures,

$$f_b = p_f \nabla n \tag{13}$$

And the solid phase stress $\boldsymbol{\sigma}_s$ is taken following the effective stress classic form,

$$\boldsymbol{\sigma}_s = \boldsymbol{\sigma}'_s - (1-n) p_f \mathbf{I} \tag{14}$$

where $\mathbf{I}$ is a 3×3 identity matrix, $\boldsymbol{\sigma}'_s$ is the effective solid phase related to the deformation of the solid phase matrix, which excludes the pressurization of the solid phase due to the pressure of the pore fluid. And the fluid phase stress $\boldsymbol{\sigma}_f$ is simplified into an isotropic pressure, $np_f\mathbf{I}$, which is expressed as,

$$\boldsymbol{\sigma}_f = -np_f \mathbf{I} \tag{15}$$

Finally, the momentum equations for solid and fluid phase are given as,

$$\bar{\rho}_s \frac{D^s \mathbf{v}_s}{Dt} = \bar{\rho}_s g - f_d + \nabla \cdot \boldsymbol{\sigma}'_s - (1-n)\nabla p_f \tag{16}$$

https://doi.org/10.5194/egusphere-2025-707
Preprint. Discussion started: 26 February 2025

$$\bar{\rho}_f \frac{D^f \mathbf{v}_f}{Dt} = \bar{\rho}_f g + f_d - n\nabla p_f \tag{17}$$

With a proper constitutive rule governing the mechanical behavior of the solid effective stress $\boldsymbol{\sigma}'_s$, the equations can fully capture the motion and physical behavior of this two-phase system.

3 Numerical implementations

3.1 Discretized of governing equations

In MPM, the material domain is discretized into Lagrangian material points under Euler background mesh. The field variables of particles can be interpolated to the background mesh nodes through shape functions. For instance, the displacement and its derivative at particle p is expressed as,

$$u_{pi} = \sum_{I=1}^{N_g} N_{Ip} u_{Ii} \tag{18}$$

$$u_{pi,j} = \sum_{I=1}^{N_g} N_{Ip,j} u_{Ii} \tag{19}$$

where subscripts i and j denote the components of tensor, which follow the Einstein summation convention, and comma between the subscripts indicates partial derivatives; u_{Ii} is the displacement at grid node I, $N_{Ip} = N_I(x_p)$ is the shape function of particle p at grid node I, x_p denotes the coordinates of particle p, $N_{Ip,j}$ is the derivative of shape functions, N_g is total the grid node number. In this study, the GIMP shape function (Bardenhagen and Kober, 2004) and discretization is used to avoid the stress oscillation promoted by the cell-crossing error.

By this way, the momentum equations are discretized in space by means of the Galerkin method considering nodal shape functions. And a discretized form of momentum equation of soil Eq. (16) on mesh node is expressed as,

$$m_{sI} a_{sIi} = f_{sIi}^{int} + f_{sIi}^{ext} \tag{20}$$

where $m_{sI} = \sum_{p=1}^{N_p} N_{Ip} m_{sp}$ is the node mass for solid, in which N_p is total the number of particles and m_{sp} is the particle solid mass; a_{sIi} is the solid acceleration at node, f_{sIi}^{int}

https://doi.org/10.5194/egusphere-2025-707
Preprint. Discussion started: 26 February 2025

and f_{sIi}^{ext} are the internal and external nodal forces, respectively.

The internal nodal force is expressed as,

$$f_{siI}^{int} = \sum_{p=1}^{N_p}(1-n_p)N_{Ip,j}\,p_{fp}V_p - \sum_{p=1}^{N_p}N_{Ip,j}\sigma'_{spij}V_p \tag{21}$$

where σ'_{spij} is the effective stress of material particle p, p_{fp} is the pore pressure of material particle, n_p is the material particle porosity, V_p is the volume of material particle p.

The external grid nodal force is expressed as,

$$f_{siI}^{ext} = \sum_{p=1}^{N_p}N_{Ip}m_{sp}b_i - \sum_{p=1}^{N_p}N_{Ip}f_dV_p + \int_{\partial\Omega}N_{Ip}\bar{\mathbf{T}}_s dS - \int_{\partial\Omega}(1-n_p)N_{Ip}\bar{\mathbf{P}}dS \tag{22}$$

where $\bar{\mathbf{T}}_s$ and $\bar{\mathbf{P}}$ are the prescribed traction and the prescribed pressure on the boundary $\partial\Omega$, respectively; dS denotes the surface integral that is only non-zero at the boundary $\partial\Omega$.

Likewise, a discretized form of the momentum equation of fluid Eq. (17) on the mesh node can be expressed as,

$$m_{fI}a_{fIi} = f_{fIi}^{int} + f_{fIi}^{ext} \tag{23}$$

where $m_{fI} = \sum_{p=1}^{N_p}m_{fp}N_{Ip}$ the grid node mass for fluid, in which m_{fp} is the particle fluid mass; $f_{fIi}^{int} = \sum_{p=1}^{N_p}n_pN_{Ip,j}\,p_{fp}V_p$ represents the nodal internal force from pore pressure gradient, $f_{fIi}^{ext} = \sum_{p=1}^{N_p}N_{Ip}m_{sp}b_i + \sum_{p=1}^{N_p}N_{Ip}f_dV_p - \int_{\partial\Omega}n_pN_{Ip}\bar{\mathbf{P}}dS$ denotes the nodal external forces from body force, inter-phase drag force and the boundary prescribed pressure, a_{fIi} is the fluid phase acceleration at mesh node, b_i is the body force vector.

Meanwhile, the strain rate associated with the material point is calculated with its corresponding nodal velocity,

$$\dot{\varepsilon}_{spij} = \sum_{I=1}^{n_g}[N_{Ip,j}v_{si} + (N_{Ip,j}v_{si})^T]/2 \tag{24}$$

$$\dot{\varepsilon}_{fpij} = \sum_{I=1}^{n_g}[N_{Ip,j}v_{fi} + (N_{Ip,j}v_{fi})^T]/2 \tag{25}$$

https://doi.org/10.5194/egusphere-2025-707
Preprint. Discussion started: 26 February 2025

where v_{si} and v_{fi} are the nodal velocity for the solid phase and fluid phase, respectively; $\dot{\varepsilon}_{spij}$ and $\dot{\varepsilon}_{fpij}$ are the particle strain rate for the solid phase and fluid phase, respectively.

3.2 Numerical stability

As mentioned above, the solid-fluid coupling MPM suffers from the volumetric locking. The stabilized technique is needed for the stability of the simulation. Here, to mitigate the pore pressure oscillation and maintain the numerical stability, the strain smoothing method is used to smooth the particle volumetric strain rate, while the pore pressure increasement at particles is calculated based on the multi-field variational principle for the stability, accuracy and smoothness of the results.

3.2.1 Strain smoothing method

The numerically stress/strain smoothing method has been used in the two-phase saturated and unsaturated MPM formulations (Lei et al., 2020; Wang et al., 2023a) and can effectively mitigate the stress oscillation in a simple way. Here, for simplicity and efficiency, a cell-based average approach (Mast et al., 2012) is employed to smooth the particle volumetric strain rate. By doing this, the volumetric strain rate of material points p is replaced by the averaged field value of the cell c which it belongs,

$$\alpha_p = \sum_{p \in c} \alpha_p m_p / \sum_{p \in c} m_p \tag{26}$$

where α_p represents the variables include the volumetric strain rate of solid and fluid, m_p is the mass of material point, representing the solid or fluid mass in different phases.

From the averaged volumetric strain rates $\bar{\varepsilon}_v$, the updated strain rates $\tilde{\dot{\varepsilon}}_{ij}$ is computed by means of,

$$\tilde{\dot{\varepsilon}}_{ij} = \dot{\varepsilon}_d + \bar{\varepsilon}_v \delta_{ij} / 3 \tag{27}$$

where $\dot{\varepsilon}_d$ is the deviatoric strain rate, δ_{ij} is the Kronecker delta. On the basis of the modified strain rates, stresses can be directly computed using the constitutive relation.

3.2.2 The multi-field variational principle

https://doi.org/10.5194/egusphere-2025-707
Preprint. Discussion started: 26 February 2025

Since the formulation of MPM is similar to the traditional FEM, the similar techniques used in FEM for volumetric locking are also applicable to the MPM. The multi-field variational principle is a commonly used anti-locking technique in the finite element method (FEM) without using high-order shape functions. In MPM, Chen et al. (Chen et al., 2018) first used the multi-field variational principles to mitigate volumetric-locking and numerical oscillation in weakly compressible problems. And then Liu et al. (Liu et al., 2020) and Tang et al. (Tang et al., 2024) applied this technique in the sing-point two phase unsaturated MPM formulation to mitigate volumetric-locking and carried out the simulation of the Hong Kong Tsui Load landslide and Yanyuan landslide. Zheng et al. (Zheng et al., 2021, 2022) used the multi-field variational principles for the patch recovery of pore pressure increment in the explicit two-point two phase MPM formulation and fully implicit MPM formulation. Based on the multi-field variational principle, the pore pressure field is approximated by expressing the pore pressure increment and the test function as (Chen et al., 2018),

$$\dot{p}_f(\mathbf{x},t) = Q^T(\mathbf{x})a(t) \tag{28}$$

$$\delta\dot{p}_f(\mathbf{x},t) = \delta a^T(t)Q(\mathbf{x}) \tag{29}$$

where $\boldsymbol{Q}$ and $\boldsymbol{a}$ are the polynomial basis function and coefficient vector to be solved. The polynomial basis function can be constant, linear, or quadratic (i.e., $\boldsymbol{Q}$ = [1], [1, x, y, z], or [1, x, y, z, x^2, xy, y^2, yz, z^2, zx], and the corresponding coefficient a = [a_0], [a_0, a_1, a_2, a_3]$^{\mathrm{T}}$, or [a_0, a_1, a_2, a_3, a_4, a_5, a_6, a_7, a_8, a_9, a_{10}]$^{\mathrm{T}}$). Here, in the single-point two-phase MPM formulation, the weak form of the pore pressure rate can be expressed as,

$$\int_\Omega \delta\dot{p}_f(\dot{p}_f + \frac{K_f}{n}[(1-n)\nabla\cdot\mathbf{v}_s + n\nabla\cdot\mathbf{v}_s]d\Omega = 0 \tag{30}$$

And then, the weak form can be changed to,

$$\int_\Omega Q\frac{K_f}{n}[(1-n)\nabla\cdot\mathbf{v}_s + n\nabla\cdot\mathbf{v}_s]d\Omega = -a\int_\Omega QQ^T d\Omega \tag{31}$$

The coefficient can be further expressed as,

$$a = -\mathbf{H}^{-1}\int_\Omega Q\frac{K_w}{n}[(1-n)\nabla\cdot\mathbf{v}_s + n\nabla\cdot\mathbf{v}_s]d\Omega \tag{32}$$

https://doi.org/10.5194/egusphere-2025-707
Preprint. Discussion started: 26 February 2025

where $\mathbf{H} = \int_{\Omega} QQ^T d\Omega$. In order to solve the coefficient vector, the node-based method (Mast et al., 2012) is used due to its simplicity and efficiency. Using the node-based method, the node coefficient vector is written as,

$$\mathbf{a}_I = -\mathbf{H}_I^{-1} \sum_{p=1}^{n_p} N_{Ip} Q_p \frac{K_f}{n} [(1-n)\nabla \cdot \mathbf{v}_s + n\nabla \cdot \mathbf{v}_s] V_p \tag{33}$$

where $\mathbf{H}_I = \sum_{p=1}^{n_p} Q_p Q_p^T N_{Ip} V_p$. After solving the coefficient vector for each node, the changing rate of pore pressure can be written as

$$\dot{p}_{fp} = Q_p^T \sum_{I=1}^{n_g} a_I N_{Ip} \tag{34}$$

where $\sum_{I=1}^{n_g} a_I N_{Ip}$ is the node value interpolated to the particle.

3.3 Numerical algorithm

https://doi.org/10.5194/egusphere-2025-707
Preprint. Discussion started: 26 February 2025

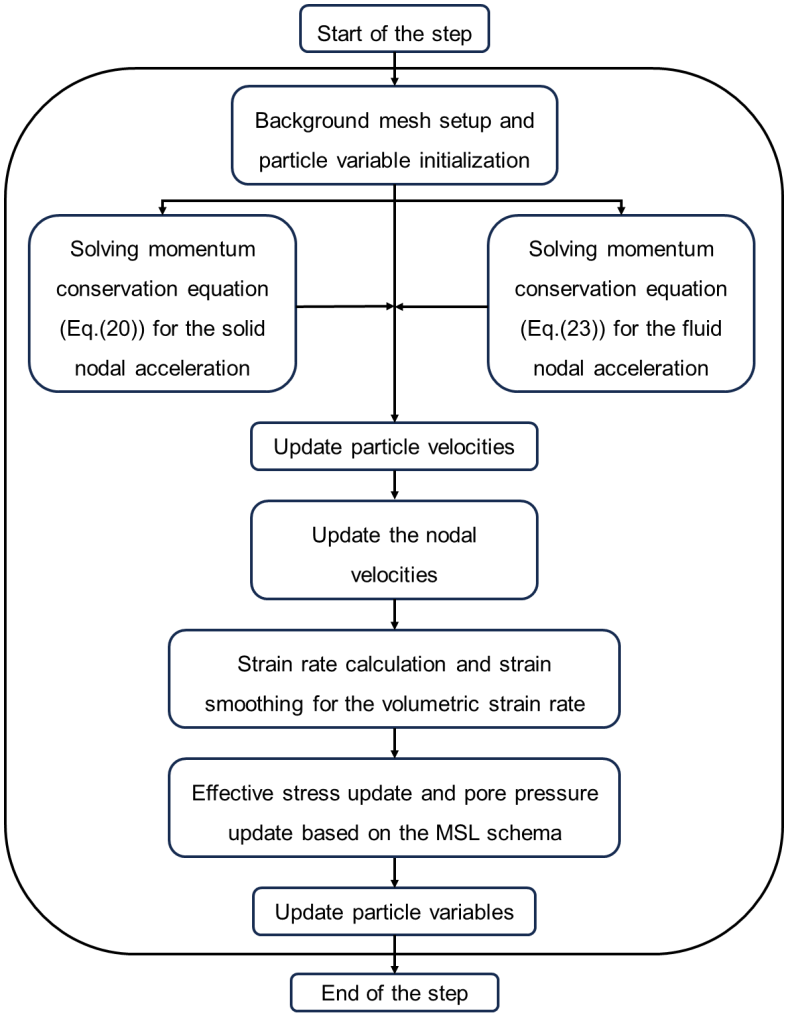

Figure 3. Numerical implementation procedure of the proposed stabilized two phase MPM formulation.

In the proposed formulation, each time step is solved explicitly according to the following sequence of sub-steps (see Fig. 3):

(1) All the variables associated with each material point are initialized first (initial position, stress, pore pressure, etc.);

(2) Interpolate the variables of material points to the nodes of the background mesh using the shape function calculated based on particle locations with respect to the background mesh nodes;

https://doi.org/10.5194/egusphere-2025-707
Preprint. Discussion started: 26 February 2025

(3) Combined with the correct boundary conditions, the accelerations of each phase on the background mesh node are obtained based on Eq. (20) and (23);

(4) Update the velocity of all material points for both phases using the FLIP scheme (Hammerquist and Nairn, 2017);

(5) Update the nodal velocities for both phases by interpolating velocities back from the material points;

(6) Strain rate increments of solid and fluid phase on particles are calculated, and the cell-based strain smoothing technique expressed in Eq. (26) is applied to smooth the volumetric strain rate;

(7) Update the effective stress based on its constitutive model and the pore pressure based on the multi-field variational principle;

(8) Update the state variables at particles, such as particle volume, porosity and position;

(9) Reset the background mesh for the next step and store all the updated information in material points.

4 Numerical examples

In this section, four numerical examples are provided to demonstrate the performance of the proposed MPM formulation. First, a one-dimensional consolidation under both small and large conditions is simulated. Subsequently, the two-dimensional consolidation under local loading and the cyclic loading test are conducted to show its efficacy under external loading. And then, the self-wight consolidation is analyzed to illustrate its capability in simulating undrained and drained conditions, as well as large deformation situation.

4.1 One-dimensional consolidation

The one-dimensional consolidation problem has been frequently studied to verify and assess numerical methods, as it allows a direct comparison with analytical solutions. Here, both small and large deformation conditions are conducted and the numerical results are compared with their corresponding analytical solutions.

https://doi.org/10.5194/egusphere-2025-707
Preprint. Discussion started: 26 February 2025

4.1.1 Small deformation

As shown in Fig. 4, a saturated soil column with a width of 0.1 m and a length of 1.0 m is considered for the simulation. An isotropic linear elastic constitutive model is employed, with parameters detailed in Table 1. The background mesh consists of cells sized 0.05 m × 0.05 m, with 4 material points in each mesh element, resulting in a total of 160 material points. Roller normal impermeable boundary is applied to the lateral surfaces, while the bottom is fully fixed and impermeable. The top surface of the column is permeable, allowing fluid to flow out through it. The initial conditions include an excess pore pressure p_0 = 10 kPa and zero effective stress. Not considering gravity, the consolidation process begins by applying a 10 kPa traction to the top material point layer and keeping it constant during the calculation. The time step is set to be 1.0×10^{-5} s with the total simulation time of 2.0 s.

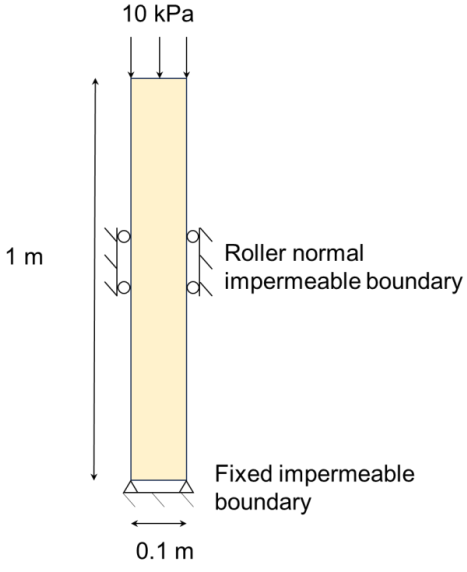

Figure 4. Schematic of the one-dimensional consolidation.

https://doi.org/10.5194/egusphere-2025-707
Preprint. Discussion started: 26 February 2025

348 **Table 1** Material parameters for the one-dimensional consolidation

Parameter	Value
Solid grain density ρ_s(kg·m^{-3})	2650
Young's modulus E (MPa)	10
Poisson's ratio υ	0.0
Fluid density ρ_w (kg·m^{-3})	1000
Initial porosity n	0.3
Bulk modulus of fluid K_f (Gpa)	2.2
Hydraulic conductivity K_s (m·s^{-1})	0.001

349

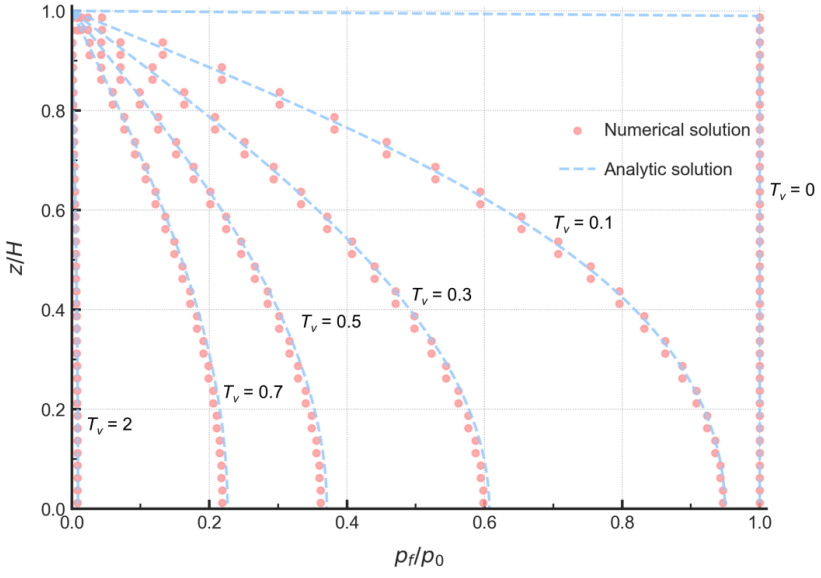

350 **Figure 5.** Comparison of pore pressure profiles from the proposed formulation with
351 Terzaghi's solution.

https://doi.org/10.5194/egusphere-2025-707
Preprint. Discussion started: 26 February 2025

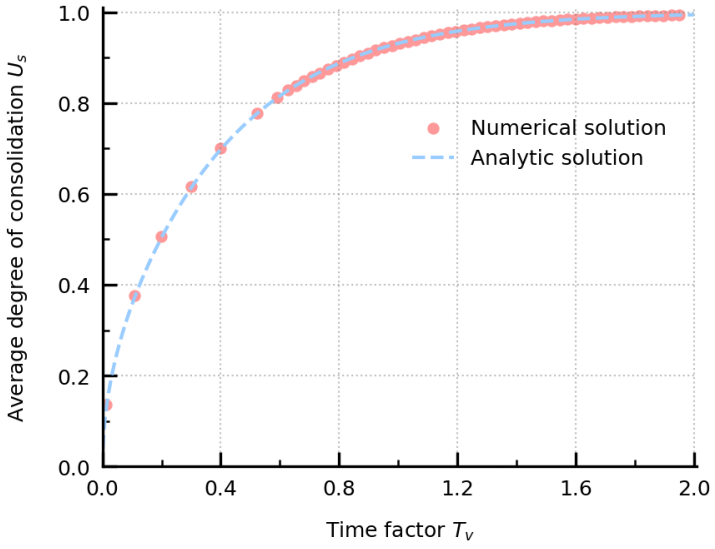

Figure 6. Comparison of the average degree of consolidation from the proposed formulation with Terzaghi's solution.

Under such a constant loading, the deformation of the column is very small and Terzaghi's one-dimensional consolidation theory is applicable. Fig. 5 presents a comparison of the normalized pore pressure distribution at different time factors between the numerical solution and the analytical solution (the time factor $T_v = C_v t / H^2$, where C_v is the coefficient of consolidation and H is the drainage path length). Initially, the pore pressure equals the external load, with the fluid phase undertaking the external loading. Since the external loading is constant, the pore fluid is gradually discharged from the top surface and the pore pressure begin to dissipate progressively from the top. The numerical results show excellent agreement with the analytical solutions, effectively capturing the dissipation process of the excess pore pressure during consolidation. Additionally, the comparison of the average consolidation degree (defined by strain) is presented in Fig. 6, indicating that the numerical results accurately replicate the deformation process as the analytical solution shows.

4.1.2 Large deformation

For the large deformation condition, the same geometry and discretization as in the

https://doi.org/10.5194/egusphere-2025-707
Preprint. Discussion started: 26 February 2025

small deformation case are used. However, a larger top traction (0.2 MPa) is applied and a softer material (E = 1MPa) is considered, and the hydraulic conductivity K_s is adjusted to be 0.0001 m·s^{-1}. Accordingly, the pore pressure is initialized at 0.2 MPa, ensuring that the loading is initially fully carried by the fluid phase. Similar to the small deformation case, after applying the constant loading, the pore pressure will gradually dissipate, but now this process will generate considerable vertical deformation. The decrease of the column-length is not negligible, therefore the small-strain Terzaghi's theory is no longer applicable. Based on the large deformation analytical solution (Xie and Leo, 2004), the evolution of pore pressure, top settlement and the average degree of consolidation (defined by strain) can be expressed as,

$$p_f(z,t) = \frac{1}{m_{vl}} \ln[1 + (e^{m_{vl} p_a} - 1) \sum_{m=1}^{\infty} \frac{2}{M} \sin(\frac{Mz}{H}) e^{-M^2 T_v}] \quad (35)$$

$$S_t = H_0 (1 - e^{-m_{vl} p_a})(1 - \sum_{m=1}^{\infty} \frac{2}{M^2} e^{-M^2 T_v}) \quad (36)$$

$$U_s = 1 - \sum_{m=0}^{\infty} \frac{2}{M^2} e^{-M^2 T_v} \quad (37)$$

where m_{vl} = 1 / E is the one-dimensional compressibility, p_a is applied external load, H_0 is the initial depth of the column, z is the distance to the top surface. With the same time step, the total simulation time is 300.0 s.

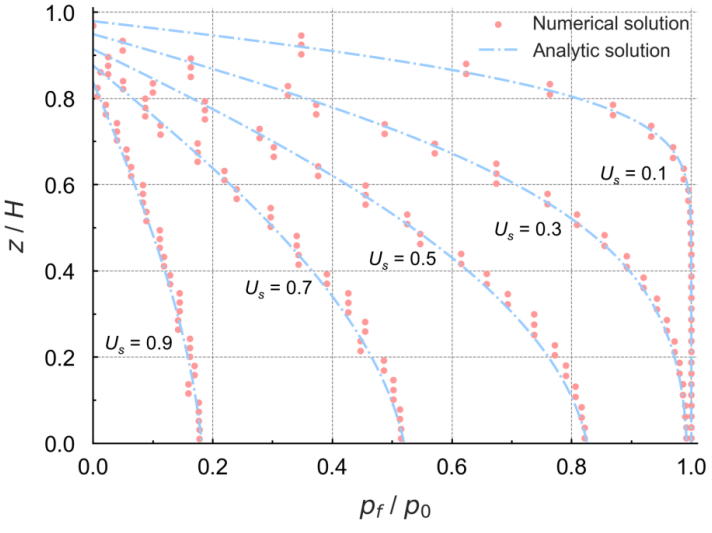

Figure 7. Comparison of pore pressure profiles from the proposed formulation with analytic solution.

https://doi.org/10.5194/egusphere-2025-707
Preprint. Discussion started: 26 February 2025

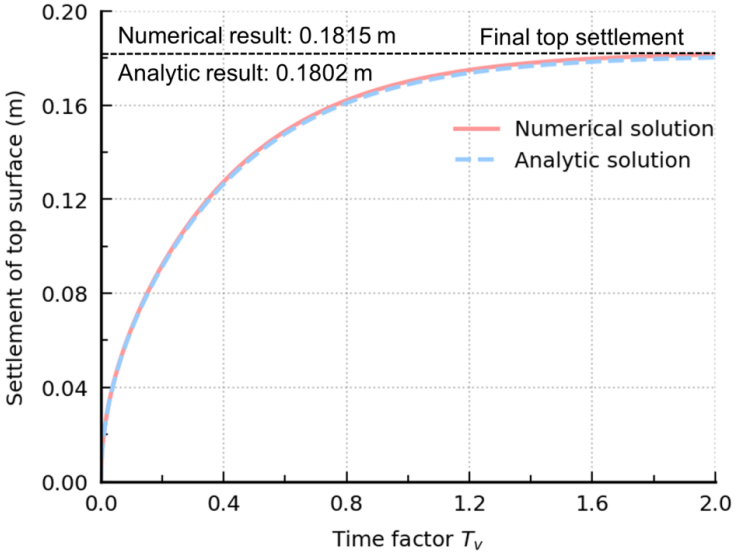

Figure 8. Comparison of the top settlement from the proposed formulation with analytic solution.

Fig. 7 shows the numerical solution of pore pressure evolution along the column height against the results from the analytic solution at different average degrees of consolidation. In the small deformation case, the consolidation coefficient C_v is equal to 1. While for the large deformation case, the consolidation coefficient C_v is very small, so the consolidation is a long process. Hence, the pore pressure dissipation here is much slower than that in the small deformation case. The comparison shows that the numerical results are consistent with the analytic solutions and accurately depict this large deformation consolidation process. The cell average method used in the strain smoothing method will give the same volumetric strain rate for the particles in the same mesh cell, resulting in the same pore pressure distribution in each mesh cell, but the overall trend of this large consolidation process can still be captured. And Fig. 8 shows the evolution of the settlement at the top surface. The numerical result (final top settlement: 0.1815 m) is very close to the analytic result (final top settlement: 0.1802 m). The comparison demonstrates the validation and applicability of the proposed formulation in this two-phase large deformation process.

https://doi.org/10.5194/egusphere-2025-707
Preprint. Discussion started: 26 February 2025

4.2 Two-dimensional consolidation under local loading

In this section, a two-dimensional elastic consolidation under a localized loading is simulated, with the geometry and boundary conditions illustrated in Fig. 9. Due to the symmetry of the problem, only half of the domain is modeled. The saturated material domain possesses a dimension of 10.0 m × 10.0 m, while the background mesh consists of cell elements sized 0.05 m × 0.05 m, with 4 material points in each cell element, resulting in 1600 particles. Roller normal impermeable boundary is applied to the lateral surfaces and the bottom, while the top surface is permeable and unconstrained. Initially, a constant local loading of 20.0 kPa, spanning a width of 0.3 m, is applied on the left side of the top surface. Without considering gravity, the initial stress and pore pressure are set to be zero. The isotropic linear elastic constitutive model is used and the material parameters are provided in Table 2. The time step of the simulation is 2.0×10^{-4} s. The same simulation has been conducted in the previous studies by semi-implicit MPM scheme (Yuan et al., 2023; Kularathna et al., 2021).

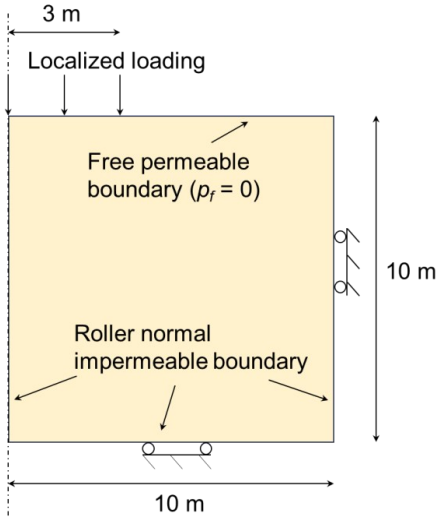

Figure 9. Model setup for the two-dimensional consolidation.

https://doi.org/10.5194/egusphere-2025-707
Preprint. Discussion started: 26 February 2025

426 **Table 2** Material parameters for the two-dimensional consolidation

Parameter	Value
Solid density ρ_s(kg·m^{-3})	2700
Young's modulus E (MPa)	10
Poisson's ratio υ	0.3
Fluid density ρ_w (kg·m^{-3})	1000
Initial porosity n	0.3
Bulk modulus of fluid K_w (Gpa)	2.2
Hydraulic conductivity K_s (m·s^{-1})	0.0001

427 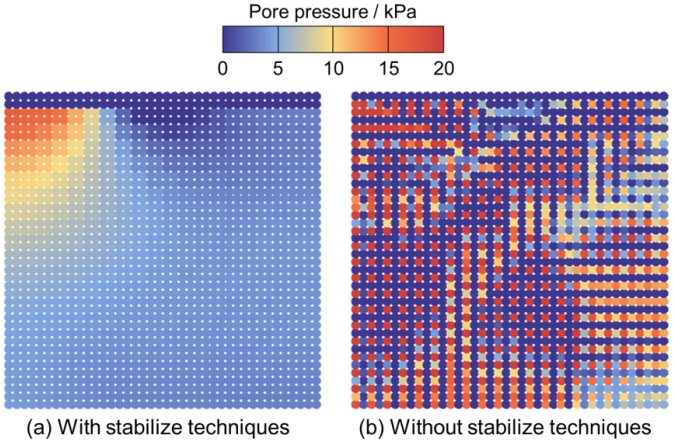

428 **Figure 10.** Pore pressure distribution with stabilize techniques and without stabilize
429 techniques at t = 0.1 s.

430 Fig. 10 illustrates the distribution of pore pressure at time t = 0.1 s, comparing results
431 with and without stabilized techniques. In Fig. 10b, a spurious pore-pressure field
432 with a checkerboard distribution is observed. In contrast, the result with stabilized
433 techniques shows a smooth excess pore pressure field caused by the external loading
434 (Fig. 10a). It demonstrates that the stabilized techniques can well mitigate pore
435 pressure oscillation in the two phase MPM formulation, offering a stable pressure
436 distribution. And the displacement distribution at t = 0.1 s is shown in Fig. 11.
437 Consistent with the applied local loading, the displacement mainly occurs in the local
438 loading region, indicating that the local loading is undertaken by the upper left corner
439 area. The maximum displacement (6.737 mm) occurs at top left corner, which is

https://doi.org/10.5194/egusphere-2025-707
Preprint. Discussion started: 26 February 2025

consistent with the result from the semi-implicit MPM formulation (Yuan et al., 2023). Similar results are also obtained using the semi-implicit MPM with artificial compressibility stabilization and fractional–step method (Yuan et al., 2023; Kularathna et al., 2021). The stabilized techniques employed here can yield equivalent results that are free of stress oscillations while accurately preserving the mechanical behavior.

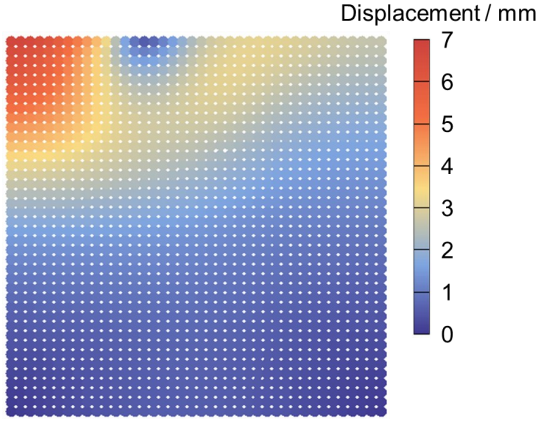

Figure 11. Distribution of displacement field at time t = 0.1 s.

4.3 Cyclic loading test

Inspirited by the lateral cycle loading test (Liang et al., 2023), we conduct a vertical cyclic loading test of a saturated granular material. The model setup is shown in Fig. 12, where the saturated material is placed in a rigid box and subjected to a vertical cyclic loading. The material domain measures 2 m in width and 1 m in height, and is discretized by quadrilateral element with size of 0.05 m × 0.05 m. And there are 4 particles in each element, giving 3200 particles. Both the bottom and laterals are normal impermeable and supported by rollers, and the top is unconstrained and permeable. To apply a cycle loading, the top surface is prescribed by a sinusoidal function periodic load of $40sin5\pi t$ kPa. Table 3 lists the material parameters used for the isotropic linear elastic constitutive model. Before the cyclic stimulation, an equilibrium condition is achieved by a linear gravity loading from 0 to 9.81 m/s^2 within $0 \leq t \leq 0.1$ s, and then the gravity remains constant. And to monitor the cycle

https://doi.org/10.5194/egusphere-2025-707
Preprint. Discussion started: 26 February 2025

loading response, three monitoring points located at the bottle, middle and top of the material domain (A, B, C) are selected (as shown in Fig. 12). The time step is set to be 1.0×10^{-5} s, and the simulation is terminated at 2.1 s.

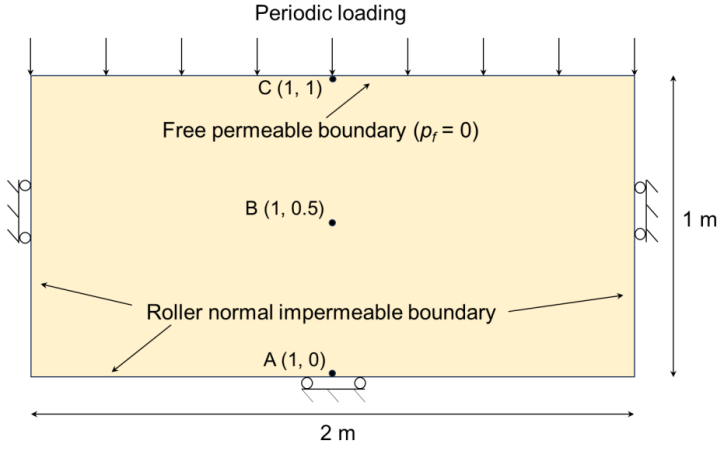

Figure 12. Schematic of cycle loading test.

Table 3 Material parameters for the cycle loading test

Parameter	Value
Solid density ρ_s(kg·m^{-3})	2650
Young's modulus E (MPa)	600
Poisson's ratio υ	0.3
Fluid density ρ_w (kg·m^{-3})	1000
Initial porosity n	0.23
Bulk modulus of fluid K_w (Gpa)	2.2
Hydraulic conductivity K_s (m·s^{-1})	0.001

https://doi.org/10.5194/egusphere-2025-707
Preprint. Discussion started: 26 February 2025

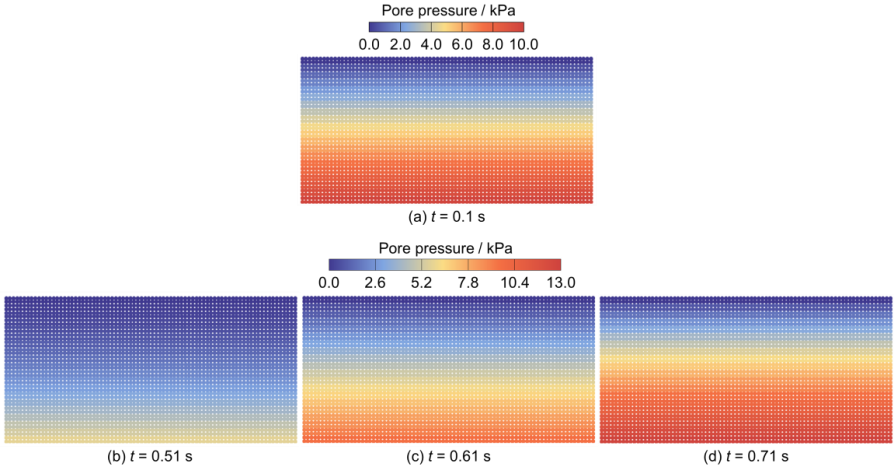

Figure 13. Distribution of pore pressure at $t = 0.1$ s (hydrostatic Pressure), $t = 0.51$ s, $t = 0.61$ s, and $t = 0.71$ s.

Fig. 13 shows the generated pore pressure at four different time instants. After the application of linear gravity loading, an equilibrium condition is achieved and a hydrostatic pressure field is generated (Fig. 13a). Subsequently, a vertical cyclic loading is applied to the surface. When the material domain is subjected to compressive loading, the pore pressure field increases, whereas under tensile loading, the pore pressure field decreases correspondingly. This vertical cyclic shaking induces an apparent periodic buildup and dissipation of excess pore pressure in the material domain. In Fig. 13b, a clear pore pressure decrease due to tensile loading at $t = 0.51$ s can be seen. As the tensile loading gradually decreases and shifts into a compressive loading, the pore pressure will gradually raise up. As a result, the pore pressure field returns to the hydrostatic state at $t = 0.61$ s (Fig. 13c). Subsequently, the compressive loading leads to a further increase in pore pressure. As depicted in Fig. 13d, a significant excess pore pressure field is regenerated. Therefore, the pore pressure in the material domain exhibits periodic variations in response to the cyclic loading.

And to further present the cyclic dynamic response under the applied cyclic loading, the evolution of pore pressure and displacement at the selected monitoring points is presented in Fig. 14. The time history of pore pressure and displacement over time demonstrates this cyclic loading response more quantitatively and vividly. The linear

https://doi.org/10.5194/egusphere-2025-707
Preprint. Discussion started: 26 February 2025

gravity loading ends at t = 0.1 s, during which the displacement remains very small. After that, the vertical loading will induce a relatively large displacement. Under the sinusoidal periodic loading, the vertical displacement of point B and C exhibits a sinusoidal variation, and the pore pressure at point A and B also changes accordingly. It can be seen that these cyclic responses can be well captured by the proposed stabilized MPM formulation.

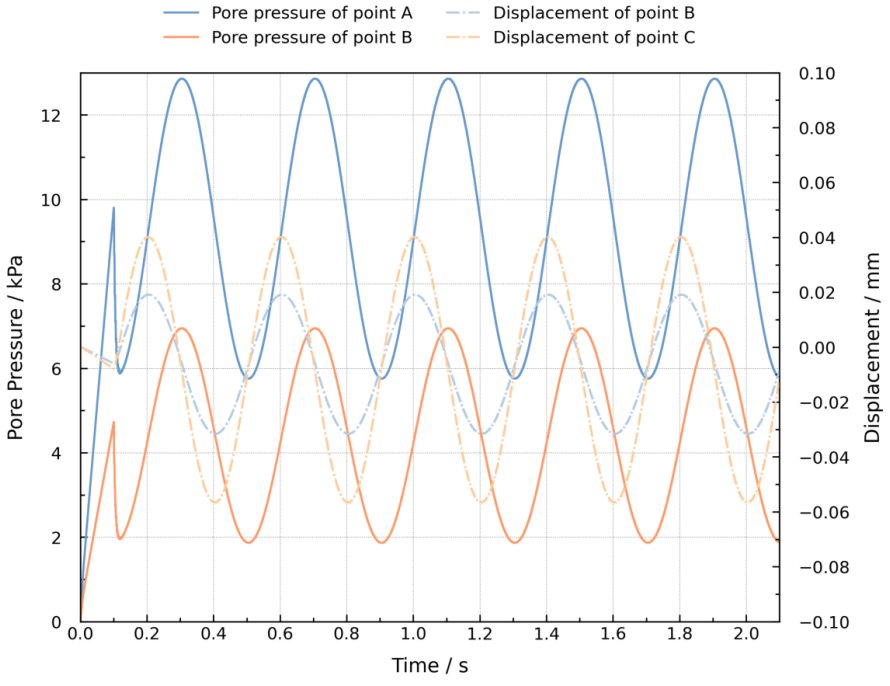

Figure 14. Evolution of pore pressure and displacement at selected points.

4.4 Self-weight consolidation

The large-deformation consolidation of an elastic slumping block under gravity loading is presented in this section (Fig. 15), which is related to the settlement of a very soft soil and has been simulated in previous studies (Zheng et al., 2021, 2022; Sang et al., 2024; Wang et al., 2023a). The simulation focuses on the right half of a symmetric domain with dimensions of 4 m width and 2 m height. The material domain is discretized using quadrilateral element of size 0.125 m× 0.125 m, and 4 particles in each element, giving 1024 particles in total. No external load is applied,

https://doi.org/10.5194/egusphere-2025-707
Preprint. Discussion started: 26 February 2025

making the consolidation process solely driven by the initial gravitational force at the start of the simulation. The gravity linearly increases from 0 to 9.81 m/s^2 within $0 \leq t \leq 0.1$ s and then remains constant. Both the top and right boundaries are unconstrained and freely draining, while the left and bottom boundaries are normal impermeable and supported by rollers. The gravity will give rise to pore pressure build-up, while the deformation will lead to the dissipation of pore pressure over time. And two points (P_1, P_2) at the bottle and middle are selected to evaluate the consolidation process (as shown in Fig. 15). An isotropic linear elastic constitutive model is used and the parameters are listed in Table 4. The total simulation time is 0.5, and the simulation is performed with a time step equal to 1.0×10^{-6} s.

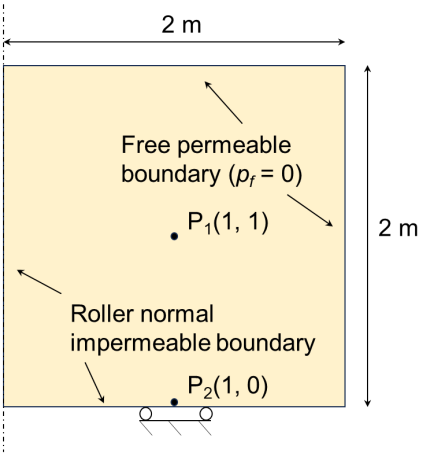

Figure 15. Schematic of the self-weight consolidation

Table 4 Material parameters for the self-weight consolidation

Parameter	Value
Solid density ρ_s(kg·m^{-3})	2650
Young's modulus E (kPa)	100
Poisson's ratio υ	0.3
Fluid density ρ_w (kg·m^{-3})	1000
Initial porosity n	0.4
Bulk modulus of fluid K_w (Gpa)	2.2
Hydraulic conductivity K_s (m·s^{-1})	0.0001

https://doi.org/10.5194/egusphere-2025-707
Preprint. Discussion started: 26 February 2025

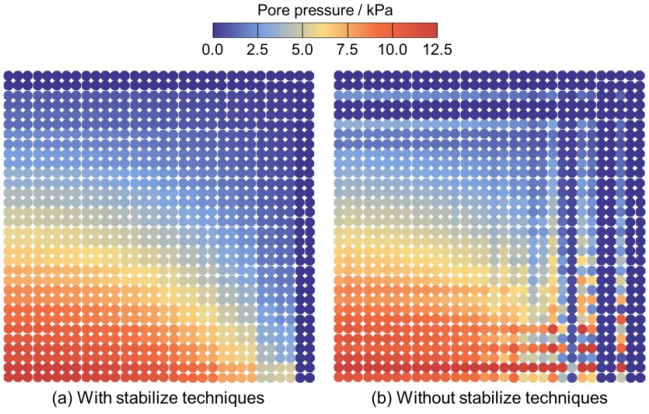

Figure 16. Pore pressures distribution at t = 0.05 s obtained with stabilize techniques and without stabilize techniques.

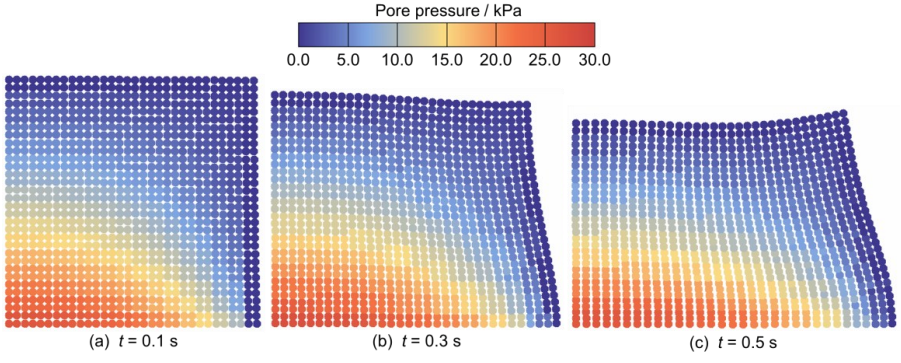

Figure 17. Pore pressures distribution at different times.

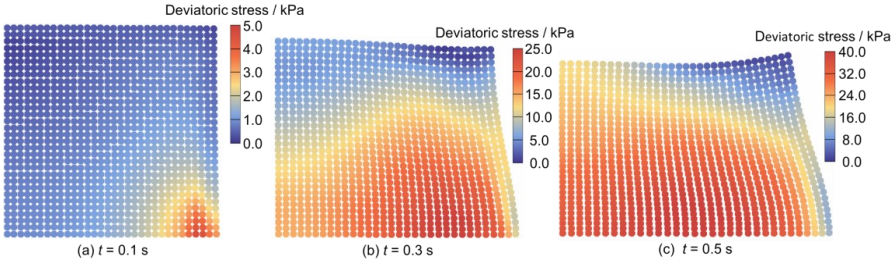

Figure 18. Deviatoric stress distribution at different times.

Initially, due to the relatively quick application of gravity loading, the pore fluid cannot be rapidly discharged and the loading process is carried out under approximately undrained condition. Therefore, the applied gravity loading will induce

https://doi.org/10.5194/egusphere-2025-707
Preprint. Discussion started: 26 February 2025

excess pore pressure at the beginning. Fig. 16 shows pore pressure fields after gravity loading (t = 0.05 s) with stabilized techniques and without stabilized techniques. One can see that the result without stabilized techniques suffers from pore pressure oscillations. The stabilized result, in contrast, eliminates spurious oscillations effectively under the stringent undrained condition. Moreover, the distribution of pore pressure and deviatoric stress at three different times (0.1 s, 0.3 s and 0.5 s) are illustrated in Fig. 17 and 18, respectively. Upon the application of linear gravity loading, a pore pressure field develops, gradually decreasing from the bottom left corner upwards, as shown at t = 0.1 s (Fig. 17a). At this stage, the deformation is not large, with a localized region of deviatoric stress distribution observed near the bottom right corner (Fig. 18a). Subsequently, gravity continues to generate pore pressure, and the deviatoric stress gradually increases as deformation progresses. As the deformation develops under gravity, the pore pressure first reaches the maximum value and then dissipates because of the deformation and drainage at the boundary. This process can be observed in Fig. 17b, Fig. 18b and Fig. 17c, Fig. 18c. Both the pore pressure and deviatoric stress filed change continuously along the large deformation process. The absence of checkerboard oscillations shows the stability of the proposed stabilized formulation in capturing the mechanical behavior of the slumping block during the consolidation process.

To further verify the accuracy of the results, the time evolution of the pore pressure at two points (P_1, P_2 in Fig. 15) is shown in Fig. 19, and the results are compared with those of Zheng et al. (Zheng et al., 2022) using implicit stabilized MPM formulation and Sang et al. (Sang et al., 2024) using implicit coupled MPM formulation. During the linear gravity loading, pore pressure increases linearly, followed by non-monotonic dissipation due to the Mandel-Cryer effect. The curves obtained using the proposed stabilized formulation agree well with those of Zheng et al. (Zheng et al., 2022) and Sang et al. (Sang et al., 2024). And the final displacement field (Fig. 20) closely matches the results reported in previous studies (Wang et al., 2023a; Yuan et al., 2023).

https://doi.org/10.5194/egusphere-2025-707
Preprint. Discussion started: 26 February 2025

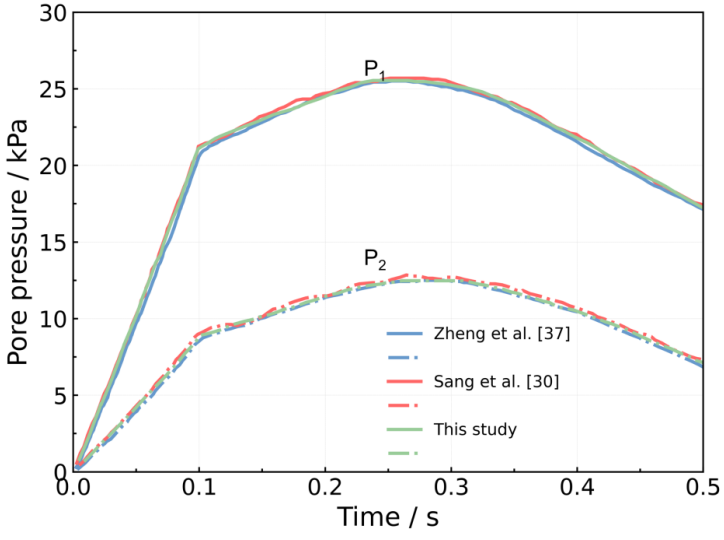

Figure 19. Pore pressures evolution at two selected points.

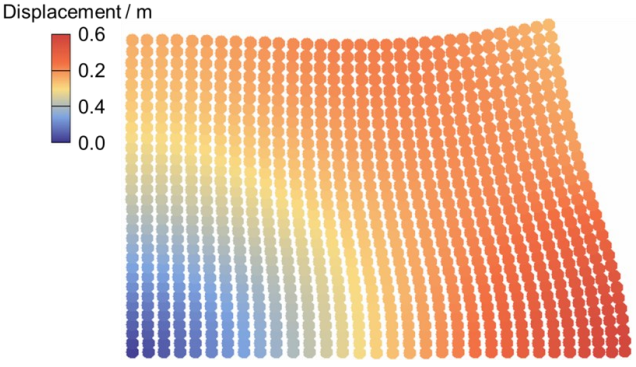

Figure 20. Displacement distribution at 0.5 s.

5 Discussion and conclusion

This study presents an explicit stabilized two-phase material point method for hydromechanical coupling problems in solid-fluid porous media. By incorporating the strain smoothing method and the multi-field variational principle in the single-point two phase MPM scheme, the proposed formulation effectively mitigates pore pressure oscillation and maintains numerical stability. The proposed two phase MPM formulation was initially validated through one-dimensional consolidation problem under both small and large deformation cases, with the numerical results showing

https://doi.org/10.5194/egusphere-2025-707
Preprint. Discussion started: 26 February 2025

strong agreement with analytical solutions. Subsequently, the two-dimensional consolidation under local loading and the cyclic loading test were performed, demonstrating the formulation's robust capability to accurately capture dynamic responses to external loading. Finally, the self-wight consolidation was analyzed to showcase its efficacy in simulating both undrained and drained conditions, as well as handling large deformation challenges. The proposed formulation produced results that aligned closely with analytical solutions and outcomes from other approaches. Particularly, the pore pressure instabilities were greatly mitigated by the stabilized techniques, as clearly validated by the numerical results in terms of pore pressure.

With its effective and easy implemented stabilized techniques, the proposed formulation is well-suited for analyzing a wide range of hydromechanical processes under various undrained, drained, and loading conditions. It offers an effective and reliable approach for simulating both static and dynamic processes in solid-fluid porous media. This work is currently limited to linear elastic behavior of the solid phase. Future efforts will focus on the practice and application involving more complex large deformation problems and advanced constitutive models.

Code and data availability. The model developed in this study is based on the open source MPM code, which is available on Github: https://github.com/xzhang66/MPM3D-F90 (Zhang et al., 2016). The current version of model is available from the project website: https://zenodo.org/records/14899281 under the Creative Commons Attribution licence. The exact version of the model used to produce the results used in this paper is archived on Zenodo (Tang, 2025).

Author Contributions. XT developed the model and wrote the original draft of the paper. WL, SH, LZ and MJ supervised the early stages of the study and provided guidance. HZ, YS and ZH have actively contributed to the formal analysis, as well as the writing and review of the paper. All authors were actively involved in the writing process.

Competing interest. There are no known conflicts of interest associated with this publication.

https://doi.org/10.5194/egusphere-2025-707
Preprint. Discussion started: 26 February 2025

Financial support. This work was supported by the National Key Research and Development program of China (Project No. 2022YFF0800604), the Major Program of the National Natural Science Foundation of China (Grant No. 42090051), and the China Scholarship Council (202304910567).

References

Bandara, S. and Soga, K.: Coupling of soil deformation and pore fluid flow using material point method, Comput. Geotech., 63, 199-214, https://doi.org/10.1016/j.compgeo.2014.09.009, 2015.

Bandara, S., Ferrari, A., and Laloui, L.: Modelling landslides in unsaturated slopes subjected to rainfall infiltration using material point method, Int. J. Numer. Anal. Methods Geomech., 40, 1358-1380, https://doi.org/ 10.1002/nag.2499, 2016.

Bardenhagen, S. G. and Kober, E. M.: The Generalized Interpolation Material Point Method, CMES-Comp Model in Eng. Sci., 5, 477–495, https://doi.org/10.3970/CMES.2004.005.477, 2004.

Baumgarten, A. S. and Kamrin, K.: A general fluid–sediment mixture model and constitutive theory validated in many flow regimes, J. Fluid Mech., 861, 721-764, https://doi.org/10.1017/jfm.2018.914, 2018.

Baumgarten, A. S., Couchman, B. L. S., and Kamrin, K.: A coupled finite volume and material point method for two-phase simulation of liquid–sediment and gas–sediment flows, Comput. Meth. Appl. Mech. Eng., 384, 113940, https://doi.org/10.1016/j.cma.2021.113940, 2021.

Ceccato, F., Yerro, A., and Carluccio, G. D.: Simulating landslides with the material point method: Best practices, potentialities, and challenges, Eng. Geol., 338, 107614, https://doi.org/10.1016/j.enggeo.2024.107614, 2024.

Chen, F., Li, H., Gao, Y., and Yan, H.: Two-particle method for liquid–solid two-phase mixed flow, Phys. Fluids, 35, 033317, https://doi.org/10.1063/5.0140599, 2023.

Chen, Z.-P., Zhang, X., Sze, K. Y., Kan, L., and Qiu, X.-M.: *v-p* material point method for weakly compressible problems, Comput. Fluids, 176, 170-181, https://doi.org/10.1016/j.compfluid.2018.09.005, 2018.

https://doi.org/10.5194/egusphere-2025-707
Preprint. Discussion started: 26 February 2025

de Vaucorbeil, A., Nguyen, V. P., and Hutchinson, C. R.: A Total-Lagrangian Material Point Method for solid mechanics problems involving large deformations, Comput. Meth. Appl. Mech. Eng., 360, 112783, https://doi.org/10.1016/j.cma.2019.112783, 2020.

Du, W., Sheng, Q., Fu, X., Chen, J., Wei, P., and Zhou, Y.: Post-failure analysis of landslide blocking river using the two-phase double-point material point method: a case of western Hubei, China, Bull. Eng. Geol. Environ., 82, 98, https://doi.org/10.1007/s10064-023-03122-6, 2023.

Fernández, F., Vargas, E., Muller, A. L., Sousa, R. L., and e Sousa, L. R.: Material point method modeling in 3D of the failure and run-out processes of the Daguangbao landslide, Acta Geotech., 19, 4277-4296, https://doi.org/10.1007/s11440-023-02152-4, 2023.

Guan, X. and Shi, H.: Translational momentum of deformable submarine landslides off a slope, J. Fluid Mech., 960,A23, https://doi.org/10.1017/jfm.2023.177, 2023.

Hammerquist, C. C. and Nairn, J. A.: A new method for material point method particle updates that reduces noise and enhances stability, Comput. Meth. Appl. Mech. Eng., 318, 724-738, https://doi.org/10.1016/j.cma.2017.01.035, 2017.

Jassim, I., Stolle, D., and Vermeer, P.: Two-phase dynamic analysis by material point method, Int. J. Numer. Anal. Methods Geomech., 37, 2502-2522, https://doi.org/10.1002/nag.2146, 2013.

Jerolmack, D. J. and Daniels, K. E.: Viewing Earth's surface as a soft-matter landscape, Nat. Rev. Phys., 1, 716-730, https://doi.org/10.1038/s42254-019-0111-x, 2019.

Jin, Y.-F. and Yin, Z.-Y.: Two-phase PFEM with stable nodal integration for large deformation hydromechanical coupled geotechnical problems, Comput. Meth. Appl. Mech. Eng., 392, 114660, https://doi.org/10.1016/j.cma.2022.114660, 2022.

Kularathna, S., Liang, W., Zhao, T., Chandra, B., Zhao, J., and Soga, K.: A semi-implicit material point method based on fractional-step method for saturated soil, Int. J. Numer. Anal. Methods Geomech., 45, 1405-1436, https://doi.org/10.1002/nag.3207, 2021.

https://doi.org/10.5194/egusphere-2025-707
Preprint. Discussion started: 26 February 2025

Lei, X., He, S., and Wu, L.: Stabilized generalized interpolation material point method for coupled hydro-mechanical problems, Comput. Part. Mech., 8, 701-720, https://doi.org/10.1007/s40571-020-00365-y, 2020.

Li, X., Tang, X., Zhao, S., Yan, Q., and Wu, Y.: MPM evaluation of the dynamic runout process of the giant Daguangbao landslide, Landslides, 18, 1509-1518, https://doi.org/10.1007/s10346-020-01569-2, 2020.

Li, Y., Zhang, J.-M., and Wang, R.: An explicit material point and finite volume sequentially coupled method for simulating large deformation problems in saturated soil, Comput. Geotech., 170, 106270, https://doi.org/10.1016/j.compgeo.2024.106270, 2024.

Li, Y., Hu, W., Zhou, L., Fan, Y., McSaveney, M., and Ding, Z.: Influence of soil density on the solid-to-fluid phase transition in flowslide flume experiments, Eng. Geol., 313, 106964, https://doi.org/10.1016/j.enggeo.2022.106964, 2023.

Lian, Y., Bui, H. H., Nguyen, G. D., and Haque, A.: An effective and stabilised (u–p_l) SPH framework for large deformation and failure analysis of saturated porous media, Comput. Meth. Appl. Mech. Eng., 408, 115967, https://doi.org/10.1016/j.cma.2023.115967, 2023.

Liang, W., Zhao, J., Wu, H., and Soga, K.: Multiscale, multiphysics modeling of saturated granular materials in large deformation, Comput. Meth. Appl. Mech. Eng., 405, 115871, https://doi.org/10.1016/j.cma.2022.115871, 2023.

Liu, C., Sun, Q., Jin, F., and Zhou, G. G. D.: A fully coupled hydro-mechanical material point method for saturated dense granular materials, Powder Technol., 314, 110-120, https://doi.org/10.1016/j.powtec.2017.02.022, 2017.

Liu, X., Wang, Y., and Li, D.-Q.: Numerical simulation of the 1995 rainfall-induced Fei Tsui Road landslide in Hong Kong: new insights from hydro-mechanically coupled material point method, Landslides, 17, 2755-2775, https://doi.org/10.1007/s10346-020-01442-2, 2020.

Mast, C. M., Mackenzie-Helnwein, P., Arduino, P., Miller, G. R., and Shin, W.: Mitigating kinematic locking in the material point method, J. Comput. Phys., 231, 5351-5373, https://doi.org/10.1016/j.jcp.2012.04.032, 2012.

https://doi.org/10.5194/egusphere-2025-707
Preprint. Discussion started: 26 February 2025

686 Pudasaini, S. P. and Mergili, M.: A Multi-Phase Mass Flow Model, J. Geophys. Res.-
687 Earth Surf., 124, 2920-2942, https://doi.org/10.1029/2019jf005204, 2019.
688 Sang, Q.-y., Xiong, Y.-l., Zheng, R.-y., Bao, X.-h., Ye, G.-l., and Zhang, F.: An
689 implicit coupled MPM formulation for static and dynamic simulation of saturated
690 soils based on a hybrid method, Comput. Mech., https://doi.org/10.1007/s00466-
691 024-02549-2, 2024.
692 Shen, W., Peng, J., Qiao, Z., Li, T., Li, P., Sun, X., Chen, Y., and Li, J.: Plowing
693 mechanism of rapid flow-like loess landslides: Insights from MPM modeling, Eng.
694 Geol., 335, 107532, https://doi.org/10.1016/j.enggeo.2024.107532, 2024.
695 Tang, X., Li, X., and He, S.: A stabilized two-phase material point method for
696 hydromechanically coupled large deformation problems, Bull. Eng. Geol. Environ.,
697 83, 184, https://doi.org/10.1007/s10064-024-03668-z, 2024.
698 Tang, X.: A stabilized two-phase material point method model, Zenodo,
699 https://doi.org/10.5281/zenodo.14899281, 2025.
700 Taylor-Noonan, A. M., Bowman, E. T., McArdell, B. W., Kaitna, R., McElwaine, J. N.,
701 and Take, W. A.: Influence of pore fluid on grain-scale interactions and mobility of
702 granular flows of differing volume, J. Geophys. Res.-Earth Surf., 127,
703 https://doi.org/10.1029/2022jf006622, 2022.
704 Tran, Q. A., Grimstad, G., and Ghoreishian Amiri, S. A.: MPMICE: A hybrid
705 MPM-CFD model for simulating coupled problems in porous media. Application to
706 earthquake-induced submarine landslides, Comput. Meth. Appl. Mech. Eng., 125,
707 e7383, https://doi.org/10.1002/nme.7383, 2023.
708 Wang, B., Vardon, P. J., and Hicks, M. A.: Rainfall-induced slope collapse with
709 coupled material point method, Eng. Geol., 239, 1-12,
710 https://doi.org/10.1016/j.enggeo.2018.02.007, 2018.
711 Wang, D., Wang, B., Yuan, W., and Liu, L.: Investigation of rainfall intensity on the
712 slope failure process using GPU-accelerated coupled MPM, Comput. Geotech., 163,
713 105718, https://doi.org/10.1016/j.compgeo.2023.105718, 2023a.
714 Wang, M., Li, S., Zhou, H., Wang, X., Peng, K., Yuan, C., and Li, J.: An improved
715 convected particle domain interpolation material point method for large

https://doi.org/10.5194/egusphere-2025-707
Preprint. Discussion started: 26 February 2025

716 deformation geotechnical problems, Int. J. Numer. Anal. Methods Geomech., 125,
717 e7389, https://doi.org/10.1002/nme.7389, 2023b.
718
719 Wyser, E., Alkhimenkov, Y., Jaboyedoff, M., and Podladchikov, Y. Y.: A fast and
720 efficient MATLAB-based MPM solver: fMPMM-solver v1.1, Geosc. Model Dev.,
721 13, 6265-6284, https://doi.org/10.5194/gmd-13-6265-2020, 2020.
722 Xie, K. H. and Leo, C. J.: Analytical solutions of one-dimensional large strain
723 consolidation of saturated and homogeneous clays, Comput. Geotech., 31, 301-314,
724 https://doi.org/10.1016/j.compgeo.2004.02.006, 2004.
725 Yamaguchi, Y., Makinoshima, F., and Oishi, Y.: Simulating the entire rainfall-induced
726 landslide process using the material point method for unsaturated soil with implicit
727 and explicit formulations, Landslides, 20, 1617–1638,
728 https://doi.org/10.1007/s10346-023-02052-4, 2023.
729 Yerro, A., Alonso, E. E., and Pinyol, N. M.: The material point method for unsaturated
730 soils, Géotechnique, 65, 201-217, https://doi.org/10.1680/geot.14.P.163, 2015.
731 Yuan, W., Zheng, H., Zheng, X., Wang, B., and Zhang, W.: An improved semi-implicit
732 material point method for simulating large deformation problems in saturated
733 geomaterials, Comput. Geotech., 161, 105614,
734 https://doi.org/10.1016/j.compgeo.2023.105614, 2023.
735 Yuan, W. H., Zhu, J. X., Liu, K., Zhang, W., Dai, B. B., and Wang, Y.: Dynamic
736 analysis of large deformation problems in saturated porous media by smoothed
737 particle finite element method, Comput. Meth. Appl. Mech. Eng., 392, 114724,
738 https://doi.org/10.1016/j.cma.2022.114724, 2022.
739 Zhan, Z. Q., Zhou, C., Cui, Y. F., and Liu, C. Q.: Initiation and motion of rainfall-
740 induced loose fill slope failure: New insights from the MPM, Eng. Geol., 346,
741 107909, https://doi.org/10.1016/j.enggeo.2025.107909, 2025.
742 Zhan, Z. Q., Zhou, C., Liu, C. Q., and Ng, C. W. W.: Modelling hydro-mechanical
743 coupled behaviour of unsaturated soil with two-phase two-point material point
744 method, Comput. Geotech., 155, 105224,
745 https://doi.org/10.1016/j.compgeo.2022.105224, 2023.

https://doi.org/10.5194/egusphere-2025-707
Preprint. Discussion started: 26 February 2025

Zhang, H. W., Wang, K. P., and Chen, Z.: Material point method for dynamic analysis of saturated porous media under external contact/impact of solid bodies, Comput. Meth. Appl. Mech. Eng., 198, 1456-1472, https://doi.org/10.1016/j.cma.2008.12.006, 2009.

Zhang X., Z Chen Z., Liu Y.: The material point method - a continuum-based particle method for extreme loading cases, Academic Press, 2016.

Zhao, S., Zhu, L., Liu, W., Li, X., He, S., Scaringi, G., Tang, X., and Liu, Y.: Substratum virtualization in three-dimensional landslide modeling with the material point method, Eng. Geol., 315, 107026, https://doi.org/10.1016/j.enggeo.2023.107026, 2023.

Zhao, Y. and Choo, J.: Stabilized material point methods for coupled large deformation and fluid flow in porous materials, Comput. Meth. Appl. Mech. Eng., 362, 112742, https://doi.org/10.1016/j.cma.2019.112742, 2020.

Zheng, X., Pisanò, F., Vardon, P. J., and Hicks, M. A.: An explicit stabilised material point method for coupled hydromechanical problems in two-phase porous media, Comput. Geotech., 135, 104112, https://doi.org/10.1016/j.compgeo.2021.104112, 2021.

Zheng, X., Pisanò, F., Vardon, P. J., and Hicks, M. A.: Fully implicit, stabilised, three-field material point method for dynamic coupled problems, Eng. Comput., 38, 5583-5602, https://doi.org/10.1007/s00366-022-01678-7, 2022.

Zheng, X., Wang, S., Yang, F., and Yang, J.: Material point method simulation of hydro-mechanical behaviour in two-phase porous geomaterials: A state-of-the-art review, J. Rock Mech. Geotech. Eng., 16, 2341-2350, https://doi.org/10.1016/j.jrmge.2023.05.006, 2024a.

Zheng, Y., Li, J., Zheng, X., Guo, N., and Yang, G.: Pre- and post-failure behaviour of a dike after rapid drawdown of river level based on material point method, Comput. Geotech., 170, 106269, https://doi.org/10.1016/j.compgeo.2024.106269, 2024b.